Nanoscale

ROYAL SOCIETY OF CHEMISTRY

PAPER

View Article Online
View Journal | View Issue

Cite this: *Nanoscale*, 2020, **12**, 7206

Photocatalytic CO_2 reduction of C/ZnO nanofibers enhanced by an Ni-NiS cocatalyst†

Hongzhao Deng,[a] Feiyan Xu,[a] Bei Cheng,[a] Jiaguo Yu *[a,b] and Wingkei Ho*[c]

Received 10th December 2019,
Accepted 5th March 2020

DOI: 10.1039/c9nr10451h

rsc.li/nanoscale

The photocatalytic reduction of CO_2 into valuable hydrocarbon fuels *via* solar energy is a promising strategy for carbon utilization. In the present paper, a hierarchical Ni-NiS/C/ZnO photocatalyst was prepared *via* the *in situ* photodeposition of compact Ni-NiS nanosheets onto C/ZnO electrospun nanofibers. The existence of metallic Ni and NiS was confirmed by X-ray photoelectron spectroscopy. Photoluminescence (PL) and time-resolved PL spectra revealed that the cocatalyst Ni-NiS enhanced the charge separation efficiency of the C/ZnO nanofibers. The as-prepared Ni-NiS/C/ZnO showed enhanced CO_2 reduction activity, with CO and CH_4 production rates 10 and 15 times greater than those of pristine C/ZnO under 350 W visible light illumination. The intermediates of CH_3O^-, HCHO, and $HCOO^-$ were detected by *in situ* Fourier transform infrared spectroscopy, confirming that CO_2 reduction is a complex reaction with multiple steps. The ^{13}C isotopic tracer method proved that CH_4 and CO were obtained from the reduction of CO_2 rather than from other carbon species in the environment. The amorphous carbon in C/ZnO could promote optical absorption, improve conductivity and reduce the interfacial charge transport resistance. Ni-NiS improved the electron–hole-pair separation of the C/ZnO nanofibers. The observed enhancement in photocatalytic activity was largely attributed to higher light utilization and effective electron–hole separation. This work proves that Ni-NiS is a promising cocatalyst to ZnO for photocatalytic CO_2 reduction.

1 Introduction

Society's production has made great progress since coal was widely used as a type of fuel for industrial production in the late 18th century. However, undue reliance on fossil fuel energy has brought about serious environmental and energy problems.[1] Extensive emission of greenhouse gases, especially CO_2, has deteriorated the environment, caused global warming, melted glaciers, aggravated natural disasters, and even threatened human health.[2–5] Moreover, excessive consumption of non-renewable energy has made human beings stand on the edge of life and death. Therefore, developing green, clean, and renewable alternative energy sources is an urgent undertaking. Solar energy is recognized as an energy source with great potential due to its characteristics of being abundant,[6,7] inexpensive,[8,9] and environment-friendly.[10,11] Therefore, developing ways to convert solar energy into fossil energy by utilizing CO_2 and H_2O *via* photocatalytic CO_2 reduction should be prioritized.[12,13]

ZnO has been widely studied as a photocatalyst due to its high exciton binding energy, rapid generation of electron (e_{CB-})–hole (h_{VB+}) pairs, and strong electron-migration ability.[14–19] However, three disadvantages largely hinder the large-scale application of ZnO: (a) fast recombination of charge carriers, (b) poor capacity for CO_2 adsorption, and (c) poor ability to absorb visible light.[20–22] Various efforts have been made to address these shortcomings, and several approaches, such as doping, constructing heterojunctions, developing new nanostructures, and loading with cocatalysts, have been proposed.[23–28] Among these methods, loading with a cocatalyst stands out because of its simplicity, low cost, and wide selection of materials.[29] Moreover, this method can boost photocatalytic activity by inhibiting the recombination of photogenerated e_{CB-} and h_{VB+}. Precious metals such as Au, Ag, Pd, and Pt are ideal candidates for applications as cocatalysts, but they are fairly expensive and have limited reserves.[30–33] Transition metal sulfides have recently attracted significant attention as cocatalysts in photocatalytic CO_2 reduction.[34–37] NiS, in particular, is a typical inorganic non-noble metal cocatalyst with multiple active centers, low toxicity, and a narrow

[a]*State Key Laboratory of Advanced Technology for Materials Synthesis and Processing, Wuhan University of Technology, Wuhan 430070, China. E-mail: jiaguoyu@yahoo.com; Tel: +86-27-87871029; Fax: +86-27-87879468*
[b]*School of Materials Science and Engineering, Zhengzhou University, Zhengzhou 450001, China*
[c]*Department of Science and Environmental Studies, The Education University of Hong Kong, Tai Po, N. T. Hong Kong, PR China. E-mail: keithho@ied.edu.hk*

†Electronic supplementary information (ESI) available. See DOI: 10.1039/c9nr10451h

band gap.[38–40] However, poor interfacial electron transfer capacity and stability are among its critical defects.[41] Engineering interfaces and doping conductive interface materials (mainly carbon materials) can remedy these shortcomings.[42] Reports on carbon material (*e.g.*, graphene and carbon nanotube)-modified nickel-based catalysts and cocatalysts to enhance photocatalytic activity are scarce.[43–46] Metallic Ni possesses conductivity similar to that of carbon. Thus, metallic Ni may be expected to accelerate the interfacial charge transport of NiS and ZnO.

In the present study, Ni-NiS/C/ZnO composite nanofibers were prepared by electrospinning and photodeposition. Aligned and uniformly deposited Ni-NiS as a cocatalyst favors the rapid separation of photogenerated charges, thereby enhancing photocatalytic activity. The amorphous carbon in C/ZnO nanofibers enhances light absorption and reduces the interface resistance of charge transport.[47] The current work provides an alternative approach to the use of non-precious metal cocatalysts to boost the CO_2 reduction activity of ZnO photocatalysts.

2 Experimental section

2.1 Materials and synthesis

Zinc acetate ($C_4H_6O_4Zn{\cdot}2H_2O$, 99.0%), commercial ZnO, *N*,*N*-dimethylformamide (DMF, 99.5%), thiourea (CH_4N_2S, 99.0%), nickel acetate ($C_4H_6NiO_4{\cdot}4H_2O$, 98.0%), absolute ethanol (C_2H_5OH), and Na_2SO_4 (99.0%) were purchased from Sinopharm Chemical Reagent Co. Ltd. Polyvinyl pyrrolidone (PVP, M_n = 1 300 000, K88-96) and Nafion® perfluorinated resin solution were purchased from Sigma-Aldrich. All reagents were used without further purification.

C/ZnO nanofibers were prepared by electrospinning. First, 0.72 g of zinc acetate and 0.80 g of PVP were dissolved in 4.9 mL of DMF under vigorous stirring until a homogeneous precursor solution was obtained. Then, the solution was loaded into a 10 mL plastic syringe equipped with a 0.5 mm stainless steel needle. The needle was connected to a 20 kV applied voltage source and the distance between the needle and the collector was fixed at 20 cm. The as-electrospun nanofibers were dried in a 60 °C vacuum oven for 24 h. Finally, C/ZnO nanofibers were obtained by annealing in air at 400 °C for 2 h with a heating rate of 5 °C min^{-1}.

Ni-NiS/C/ZnO composite photocatalysts were prepared by *in situ* photochemical deposition. In detail, 100 mg of C/ZnO nanofibers was added to a mixed solution of 5 mL of Ni $(CH_3COO)_2$ aqueous solution (0.05 mol L^{-1}), 5 mL of thiourea aqueous solution (0.5 mol L^{-1}), and 40 mL of a mixed solution of H_2O and ethanol (volume ratio 1 : 1). Then, the resultant suspension was bubbled with high purity N_2 for 40 min to remove air. Irradiation was carried out for a given period (20–120 min) with a 350 W Xe arc lamp (UV-visible light, average light intensity = 10 117 μW cm^{-2}) at room temperature (see ESI Fig. S1†). Finally, the ash-black products were collected by suction filtration, washed repeatedly with H_2O and alcohol, and dried in a 60 °C vacuum oven for 24 h. The content of Ni-NiS in the samples was controlled by adjusting the photodeposition time. The as-prepared Ni-NiS/C/ZnO nanomaterials were designated C-ZNNS20, C-ZNNS60, and C-ZNNS120 to indicate deposition times of 20, 60, and 120 min, respectively. C-Z and NNS represent pristine C/ZnO nanofibers and Ni-NiS, respectively. The precise contents of each element in C-ZNNS20, C-ZNNS60, and C-ZNNS120 were measured by inductively coupled plasma-atomic emission spectrometry (ICP-AES) (Table 1). Additionally, the Ni/NiS mass ratios for samples C-ZNNS20, C-ZNNS60 and C-ZNNS120 are presented in ESI Table S1.†

2.2 Characterization

The actual elemental contents of C-ZNNS20, C-ZNNS60, and C-ZNNS120 were determined through ICP-AES. X-ray diffraction (XRD) patterns were recorded on a D/Max-RB X-ray diffractometer (see ESI, Fig. S2†). Sample morphologies were observed on a JSM 7500F field emission scanning electron microscope (FESEM). Transmission electron microscopy (TEM) and energy dispersive X-ray (EDX) spectrometry were conducted on a Titan G2 60-300 electron microscope. N_2/CO_2 adsorption–desorption data were recorded on a Micromeritics ASAP 3020 N_2 adsorption apparatus (USA) at 423.15 K. Pore size distributions were determined *via* the Barret–Joyner–Halenda method using desorption data. The ultraviolet-visible (UV-Vis) diffuse reflectance spectra of samples were recorded on a Shimadzu UV-2600 spectrophotometer. X-ray photoelectron spectroscopy (XPS) measurements were conducted on a Thermo ESCALAB 250Xi instrument with Al Kα X-ray radiation. *In situ* Fourier transform infrared spectroscopy (FTIR, Nicolet iS50, TMO, USA) was used to monitor the photocatalytic CO_2 reaction process online.

Electrochemical impedance spectroscopy (EIS) and Mott–Schottky (M–S) measurements were taken using an electrochemical analyzer (CHI660C Instruments) in a standard three-electrode system in which a Pt wire and Ag/AgCl (saturated KCl) were set as the counter electrode and reference electrode, respectively. EIS measurements were carried out by applying a bias of 10 mV and recording over the frequency range of 0.01–10^5 Hz. All applied potentials were converted to that of a normal hydrogen electrode (NHE): $E_{NHE} = E_{Ag/AgCl} + 0.197$ V.

2.3 Photocatalytic reduction of CO_2

Photocatalytic reduction of CO_2 was carried out in a 200 mL home-made Pyrex reactor according to our previously reported

Table 1 Elemental contents of C, O, Zn, S, and Ni in C-ZNNS20, C-ZNNS60, and C-ZNNS120

	C (wt%)	O (wt%)	Zn (wt%)	Ni (wt%)	S (wt%)	Ni-NiS (wt%)
C-ZNNS20	8.14	17.37	71.06	2.56	0.87	3.43
C-ZNNS60	7.87	17.19	70.19	3.56	1.21	4.75
C-ZNNS120	7.71	16.84	68.77	4.99	1.69	6.68

method. A 350 W simulated solar Xe arc lamp (Zhenjian Silver Jewellery Chemical, China) was used as the light source in photocatalytic reduction of CO_2 (UV-visible light, average light intensity = 10 117 μW cm^{-2}). Blank experiments were carried out in the absences of CO_2 and/or light irradiation to confirm that CO_2 and light are the two key elements for photocatalytic CO_2 reduction. A $^{13}CO_2$ isotope tracer experiment was conducted to verify the carbon source of the products using a gas chromatography-mass spectrometer (GC-MS) (6980N Network GC System-5975 Inert Mass Selective Detector, Agilent Technologies, USA) to analyze the products. The gas chromatographic column used in the GC-MS test was a P/N 19091J-433 (Agilent) equipped with a capillary column HP-5 (length: 30 m, inner diameter: 0.32 mm, film thickness: 0.25 μm). The instrument was equipped with a flame ionization detector (FID). N_2 was used as the carrier gas during the test. The photocatalytic products were taken from the photocatalytic reactor by a 100 μL sampler and injected into the instrument for detection.

3 Results and discussion

3.1 Morphologies of the materials

The morphologies of the samples were explored using FESEM and TEM and the results are shown in Fig. 1. Pristine C-Z had smooth nanofibers with an average diameter of 400 nm (Fig. 1a and inset). Numerous Ni-NiS nanosheets grew out of the C-Z nanofibers upon photodeposition (Fig. 1b and inset). Fig. 1c reveals the existence of Ni-NiS nanosheets and confirms that Ni-NiS is tightly attached to the C-Z surface. The high-resolution TEM (HRTEM) image in Fig. 1d shows lattice spacings of 0.106 and 0.16 nm, which respectively correspond to the hexagonal ZnO (110) and rhombohedral NiS (211) facets. These results agree with the XRD results and demonstrate that Ni-NiS is indeed uniformly deposited on the C-Z nanofibers. The EDX elemental mapping of C-ZNNS60 (Fig. 1e) proves that the sample contains Zn, O, Ni, S, and C elements, thus confirming the existence of C/ZnO and Ni-NiS.

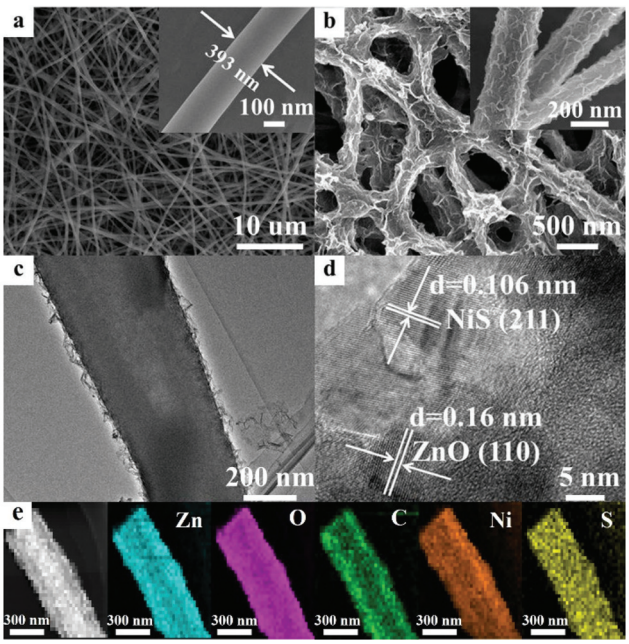

Fig. 1 FESEM images of (a) C-Z and (b) C-ZNNS60. Insets: Corresponding enlarged images. (c) TEM and (d) HRTEM images of C-ZNNS60. (e) EDX elemental mapping of C-ZNNS60.

3.2 UV-Vis diffuse reflectance spectra

The optical properties of the materials were studied to determine their optical absorption properties[48] and the results are shown in Fig. 2. Compared with commercial ZnO, C-Z could absorb UV and some near-infrared light due to its carbon content.[49] The absorption of C-ZNNS60 was greatly improved compared with that of pristine C-Z due to the dark color and narrow band gap of Ni-NiS.[50] Among the samples studied, NNS possessed the best absorption properties, mainly due to its black coloration and photothermal effects. Moreover, the higher the cocatalyst loading, the better the observed absorbance (see ESI Fig. S3†). These results indicate that adding carbon and loading with the cocatalyst favor absorption and could effectively improve the photocatalytic activity of the photocatalysts.[51]

3.3 BET and CO_2 adsorption performance of the photocatalysts

The surface area (S_{BET}), pore volume (V_p) and average pore size (d_p) of the resultant samples were measured by the N_2 sorption technique. The N_2 adsorption–desorption isotherms of C-Z, NNS, C-ZNNS20, C-ZNNS60 and C-ZNNS120 are presented in Fig. 3a. The isotherms of the five samples can be considered to be type IV isotherms. In addition, we can observe H3 type hysteresis rings from their characteristics, which generally means that there are a lot of lamellar materials forming slit holes. The pore size distributions of the different samples are illustrated in the inset of Fig. 3a. Compared with C-Z, the com-

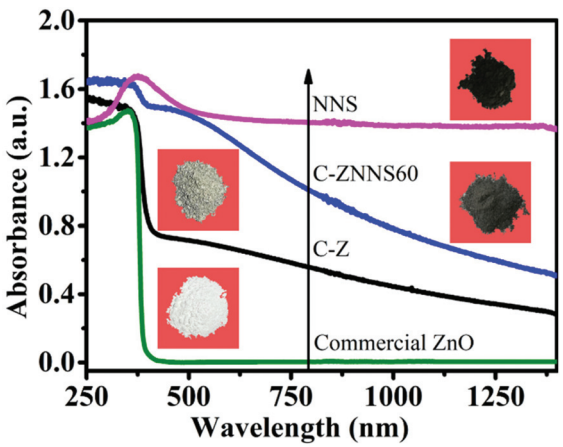

Fig. 2 UV-Vis diffuse reflectance spectra of commercial ZnO, C-Z, C-ZNNS60, and NNS.

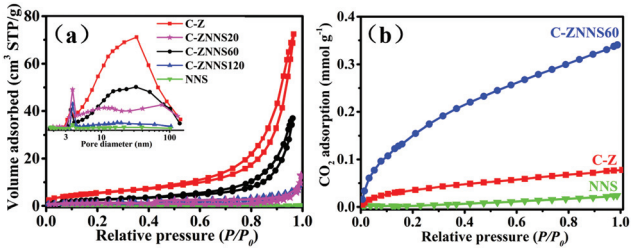

Fig. 3 (a) N_2 adsorption–desorption isotherms and pore size distribution curves (inset) of C-Z, NNS, C-ZNNS20, C-ZNNS60, and C-ZNNS120. (b) CO_2 adsorption isotherms of NNS, C-Z, and C-ZNNS60.

posites possessed more mesopores of around 3 nm, caused by the tiny slits accumulated from the Ni-NiS nanosheets.

The S_{BET}, V_p and d_p values of all the samples are listed in Table 2 and indicate that the specific surface areas of composites decrease toward C-Z. The V_p and d_p of the composite samples both decreased compared with the pristine C-Z, implying that loading of Ni-NiS changed the pore structure of the samples. Usually, a decrease of S_{BET} reduces the active sites of photocatalysts and their photocatalytic performance. However, S_{BET} is not the only factor affecting photocatalytic activity.

CO_2 adsorption isotherms (Fig. 3b) of NNS, C-Z, and C-ZNNS60 were examined to evaluate their CO_2 adsorption capability because adsorption is an initial and indispensable step for the complex CO_2 reduction process. As the relative pressure reached atmospheric pressure, NNS, C-Z, and C-ZNNS60 showed maximum CO_2 adsorption values of 0.019, 0.078, and 0.341 mmol g^{-1}, respectively. C-ZNNS60 clearly exhibits a CO_2 adsorption capacity superior to those of pristine C-Z and NNS, which could be attributed to the hierarchical structure built by C-Z and NNS in the catalyst. Ni and Ni^{2+} could also provide abundant coordination, activation, and reduction sites for CO_2 molecules. Lewis acid–base neutralization between NiS and CO_2 is a factor that must be considered.[52] Chemical adsorption facilitates CO_2 enrichment and enhances the photocatalytic activity for CO_2 reduction; these concepts will be discussed in detail later in this paper.

3.4 X-ray photoelectron spectral analysis

XPS was then used to analyze the surface chemical states of the samples. The survey spectrum of C-Z (Fig. 4a) shows the presence of C, O, and Zn elements and that of C-ZNNS60 contains C, O, Zn, Ni, and S elements. Zn was not apparent in the survey XPS spectrum of C-ZNNS60 due to the shielding effect of Ni-NiS. Additionally, S peaks became much less noticeable for C-ZNNS60, due to the too low content of Ni-NiS deposited on C/ZnO nanofibers. In fact, S element still exists according to the S 2p high-resolution spectrum of C-ZNNS60 (Fig. 4e).

Table 2 Textural properties of samples C-Z, NNS, C-ZNNS20, C-ZNNS60 and C-ZNNS120

Samples	S_{BET} [m^2 g^{-1}]	V_p [cm^3 g^{-1}]	d_p [nm]	CO_2 adsorption [mmol g^{-1}]
C-Z	23	0.09	15.7	0.08
C-ZNNS20	4	0.01	9.27	0.21
C-ZNNS60	13	0.04	14.0	0.34
C-ZNNS120	4	0.01	9.90	0.15
NNS	3	0.01	10.1	0.02

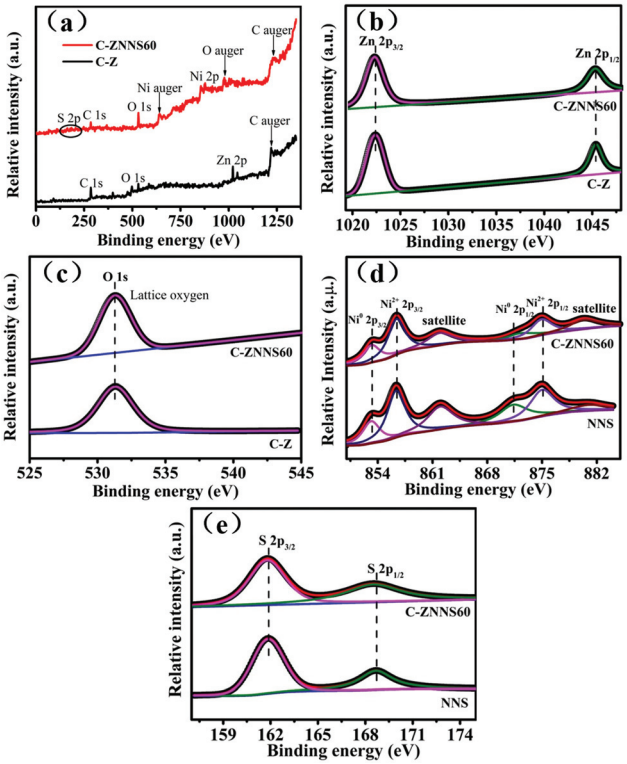

Fig. 4 (a) XPS survey spectra of C-Z and C-ZNNS60. High-resolution XPS spectra of (b) Zn 2p, (c) O 1s of C-Z and C-ZNNS60, and (d) Ni 2p and (e) S 2p of NNS and C-ZNNS60.

The Zn 2p XPS spectra (Fig. 4b) of C-Z and C-ZNNS60 show two distinct peaks at 1022.4 (Zn $2p_{3/2}$) and 1045.4 (Zn $2p_{1/2}$) eV, which correspond to Zn^{2+} in C-Z and C-ZNNS60, respectively.[53,54] The O 1s XPS spectra of C-Z and C-ZNNS60 in Fig. 4c illustrate two peaks at 529.6 and 531.5 eV, which correspond to the lattice and hydroxyl oxygen atoms in C-Z and C-ZNNS60, respectively. In Fig. 4d, which shows the Ni 2p XPS spectrum, two chemical states of Ni, namely Ni^0 (853.8 and 871.1 eV) and Ni^{2+} (857.5 and 874.8 eV), could be observed; these states directly indicate the generation of NiS and metallic Ni. In addition, two peaks located at 862 and 880.5 eV could be ascribed to the satellite peaks of Ni^{2+} $2p_{3/2}$ and Ni^{2+} $2p_{1/2}$, respectively. In the XPS spectrum of S 2p in Fig. 4e, the peaks at 161.9 and 168.7 eV correspond to S^{2-} and thioperoxydicaronimidic diamide, respectively.[55,56]

3.5 Electrochemical properties

The slope of the straight line in the M–S plot of C-Z is positive, indicating that it is an n-type semiconductor. The flat-band potential (E_{fb}) of C-Z was obtained from the M–S measure-

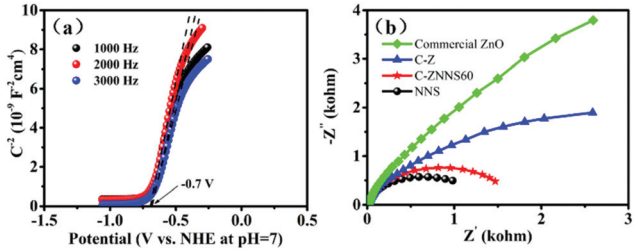

Fig. 5 (a) Mott–Schottky curves of C-Z. (b) Nyquist plots of commercial ZnO, C-Z, C-ZNNS60, and NNS.

ments in Fig. 5a. The conduction band (CB) minimum of n-type semiconductors is approximately equal to its E_{fb}. Thus, the CB level of C-Z is −0.7 V *versus* NHE at pH = 7. Given that the potentials of CO_2/CO (−0.53 V) and CO_2/CH_4 (−0.24 V) at pH = 7 are lower than the CB level of C-Z, the e_{CB-} in the CB can migrate to Ni-NiS and effectively reduce CO_2 to CO and CH_4.

EIS was performed to study the carrier-migration rate in the photocatalysts (Fig. 5b). In general, charge transport becomes more efficient as the semicircle in the Nyquist diagram becomes smaller. As shown in Fig. 5b, C-Z has a smaller arc radius relative to that of commercial ZnO; this result could be ascribed to the introduction of carbon and improvements in conductivity, which is vital evidence of the ability of carbon to reduce the interfacial charge transport resistance of the materials. NNS possesses a smaller arc radius compared with C-Z and C-ZNNS60 because of its good conductivity. In addition, the arc radius of C-ZNNS60 is smaller than that of C-Z, which indicates that *in situ* deposition of NNS reduces the interfacial electron-transfer resistance and promotes the migration ability of photogenerated e_{CB-}.

3.6 Photocatalytic CO_2 reduction and cycling performance

The photocatalytic CO_2 reduction performances of the samples were evaluated under 350 W xenon lamp illumination. Fig. 6a shows the CO and CH_4 production rates of C-Z, C-ZNNS20, C-ZNNS60, C-ZNNS120 and NNS. Control experiments showed that the target products are not produced in the absence of a photocatalyst, carbon source, or illumination. Pristine C-Z and NNS showed very low production rates of CO and CH_4 due to rapid e_{CB-}–h_{VB+} recombination. However, the photocatalytic yields of CO and CH_4 were greatly enhanced after the combination of C-Z and NNS. In addition, as the NNS loading increased, the yields of CO and CH_4 first increased and then decreased, peaking at 5.86 and 1.14 μmol g^{-1} h^{-1}, respectively. This result could be attributed to the ability of the cocatalyst to enhance the charge separation efficiency of the system at an appropriate loading content. However, overloading Ni-NiS could shield the absorption of C-Z, which is harmful to CO_2 reduction.

An isotope experiment of the photocatalytic-reduction reaction containing $^{13}CO_2$ ($^{12}CO_2$ as a reference) was conducted using GC-MS (Fig. 6b) to prove that the products CO and CH_4

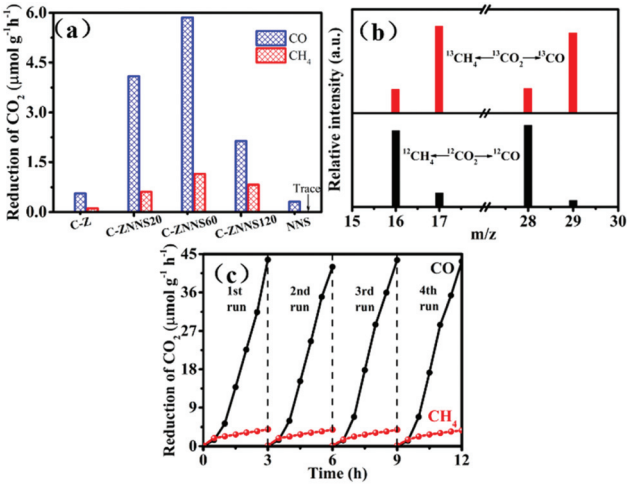

Fig. 6 (a) Photocatalytic CO_2 reduction performances of all samples. (b) CO and CH_4 mass spectra of C-ZNNS60. (c) Cyclic CO_2 reduction curves for CO and CH_4 yield (350 W, $NaHCO_3$ = 1 mmol).

originate from the CO_2 reduction reaction rather than other carbon species in the environment. When $NaH^{13}CO_3$ was used as the carbon source, $^{13}CH_4$ and ^{13}CO with m/z = 17 and m/z = 29, respectively, were the major products formed. Conversely, $^{12}CH_4$ and ^{12}CO with m/z = 16 and m/z = 28, respectively, were the major products formed when $NaH^{12}CO_3$ was used as the carbon source. These results strongly confirm that the carbon in the photocatalytic products comes from the decomposition of $NaHCO_3$ rather than pollution carbon in the environment. Cycling stability is an important factor to consider for a catalyst. Fig. 6c shows that the decline in catalyst activity is nearly negligible after four cycles of usage, which indicates the good stability of C-ZNNS60.

3.7 *In situ* Fourier transform infrared spectroscopy measurements

In situ FTIR spectroscopy of C-ZNNS60 was conducted to explore CO_2 adsorption and the reaction mechanism of the photocatalytic CO_2 reduction reaction over the Ni-NiS/C/ZnO photocatalyst. The results are shown in Fig. 7. In the absences of irradiation, H_2O and CO_2, the spectrum of C-ZNNS60, which is marked as line [a], was collected as the background. After CO_2 gas was bubbled into the reaction system for 30 and 60 min (lines [b] and [c]), peaks appeared at 1342 and 1513 cm^{-1}, which correspond to the stretching vibrations of m-CO_3^{2-}, and at 1313, 1396, and 1539 cm^{-1}, which correspond to the stretching vibrations of b-CO_3^{2-}. The intensity of most peaks was obviously enhanced after illumination, but the peak positions did not change significantly. After illumination for 30 and 60 min (lines [d] and [e]), the characteristic peaks of methoxy (CH_3O^-) (1170, 1418, and 1770 cm^{-1}), formaldehyde-based HCHO (1066, 1361, and 1716 cm^{-1}), and formic radical ($HCOO^-$) (1242, 1473, 1620, 1743, and 1793 cm^{-1}) began to appear, thus indicating that photocatalytic CO_2 reduction over C-ZNNS60 is a complicated and multi-step reaction process.[57]

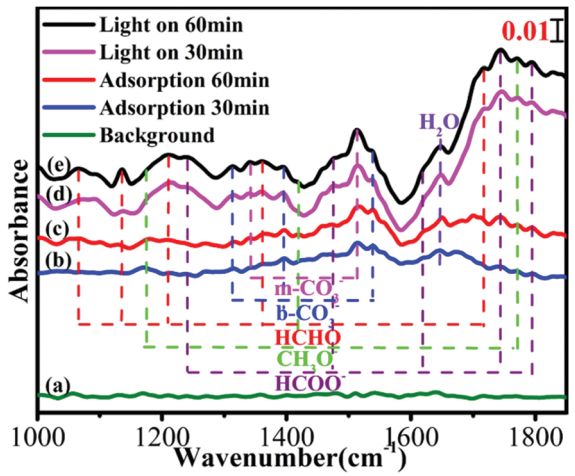

Fig. 7 *In situ* FTIR spectra of C-ZNNS60: (a) in the absence of CO_2 and H_2O in the dark, after adsorption of CO_2 and H_2O for (b) 30 min and (c) 60 min in the dark, and under light irradiation for (d) 30 min and (e) 60 min.

3.8 Photoluminescence spectral analysis

In order to further study the charge recombination and separation behaviors of the as-prepared samples, photoluminescence (PL) spectra were conducted and the results are shown in Fig. 8a.[58] Fig. 8a shows that all samples have two typical characteristic peaks at approximately 385 and 550 nm which could be attributed to the near-band-edge emission of the wide C-Z band gap and the presence of oxygen vacancies and –OH groups, respectively.[59–61] The peak at 449 nm is generated by bound excitons. Moreover, the peak at 485 nm could be attributed to Zn vacancies.[62] The PL fluorescence intensity of the composites decreased significantly compared with that of C-Z, thus indicating that the composites have a lower e_{CB-}–h_{VB+} recombination rate. The minimal fluorescence intensity of C-ZNNS60 also indicates that this sample presents the best photocatalytic performance among the catalysts. These results prove that Ni-NiS could boost the separation and transfer of charge carriers as a cocatalyst, thereby leading to high photocatalytic activity.

To explore the carrier lifetimes and decay dynamics in Ni-NiS/C/ZnO nanofibers, time-resolved PL (TRPL) spectra of C-Z, NNS and C-ZNNS60 were taken (Fig. 8b) and the average lifetimes obtained from three-exponential fitting are presented in Table 3. The average lifetime of C-ZNNS60 was the shortest among the three samples, likely because of more non-radiation transitions in this sample. The cocatalyst Ni-NiS serves as an electron sink and accelerates the separation of e_{CB-} from C/ZnO to Ni-NiS and then to CO_2. Thus, e_{CB-}–h_{VB+} recombination in C/ZnO is effectively inhibited and the photocatalytic reduction activity of CO_2 is efficiently improved.

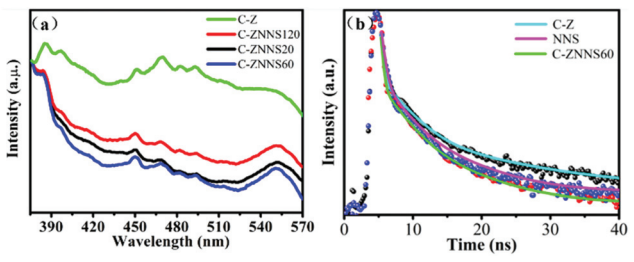

Fig. 8 (a) Photoluminescence (PL) spectra of C-Z, C-ZNNS20, C-ZNNS60, and C-ZNNS120. (b) Time-resolved PL spectra of C-Z, NNS, and C-ZNNS60.

Table 3 Average fluorescence lifetimes of the samples

	τ_1 (ns)	τ_2 (ns)	τ_3 (ns)	$\tau_{Average}$
C-Z	0.27	2.44	11.09	2.52
NNS	0.23	2.04	6.39	1.58
C-ZNNS60	0.35	1.96	6.13	1.46

3.9 Photocatalytic mechanism

According to the M–S curve, the CB potential of C/ZnO is −0.7 V *versus* NHE at pH = 7 (Fig. 5a) but the redox potential of Ni^{2+}/Ni^0 is only −0.64 V (*versus* NHE). Thus, e_{CB-} on the CB of C/ZnO possess enough reduction capacity to reduce Ni^{2+} to Ni^0 directly. First, e_{CB-} and h_{VB+} gather at the surface when C/ZnO is illuminated. Then, some of the Ni^{2+} and ethanol are reduced/oxidized to Ni^0 and acetic acid by e_{CB-} and h_{VB+}, respectively. The remaining Ni^{2+} reacts with the S^{2-} produced by the decomposition of thiourea to form NiS, which eventually forms a hierarchical structure of Ni-NiS/C/ZnO. Ni-NiS acts as a cocatalyst to promote the separation and transfer of e_{CB-} from the C/ZnO CB to itself, during which CO_2 molecules are reduced to CO and CH_4.

Based on the above results, we propose the photocatalytic mechanism shown in Fig. 9. Although the CB edge of C/ZnO (−0.7 V) is more negative than the reduction potentials of CO_2/CO (−0.53 V) and CO_2/CH_4 (−0.24 V), pristine C/ZnO reduces CO_2 with fairly low efficiency due to the rapid recombination of e_{CB-} and h_{VB+} and its poor CO_2 adsorption. When C/ZnO is modified by Ni-NiS, e_{CB-} migrate from ZnO to the electron storage carbon and cocatalyst Ni-NiS. Optimization of the

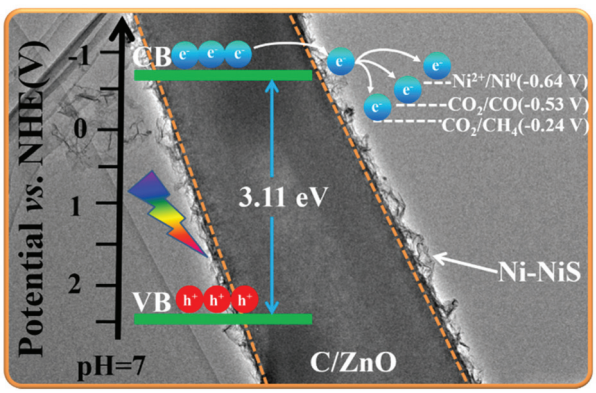

Fig. 9 Schematic diagram of photogenerated electron transfer paths in Ni-NiS/C/ZnO.

charge transport pathway effectively suppresses the recombination of e_{CB-} and h_{VB+}, thereby efficiently improving CO_2 photoreduction activity. However, increasing the concentration of cocatalyst (mass ratio Ni/NiS = 0.39) from 4.75% to 6.68% is harmful to the photocatalytic activity due to the shielding effect of Ni-NiS.

4 Conclusions

In this work, a hierarchical Ni-NiS/C/ZnO photocatalyst was prepared by photodepositing Ni-NiS nanosheets onto electrospun C/ZnO nanofibers. We found that Ni-NiS can remarkably enhance the photocatalytic CO_2 reduction activity of C/ZnO nanofibers when applied as a cocatalyst. Ni-NiS/C/ZnO favored the adsorption of CO_2 due to chemical adsorption between the cocatalyst and CO_2 molecules. Furthermore, part of the Ni^{2+} is reduced by e_{CB-} and the cocatalyst Ni-NiS is formed during sample preparation; this cocatalyst serves as an electron sink and suppresses the rapid recombination of e_{CB-} and h_{VB+} during the photocatalytic process. Hence, the Ni-NiS is confirmed to increase the adsorption of CO_2 on the cocatalyst Ni-NiS surface and promote e_{CB-} migration from C/ZnO nanofibers to the Ni-NiS nanosheets to CO_2 molecules. Amorphous carbon functions as an electron storage and electron enrichment center due to its good electrical conductivity. Additionally, it can effectively remedy the poor light utilization of ZnO by improving its absorbance and broadening its wavelength range. Moreover, the existence of amorphous carbon could reduce interfacial charge transport resistance and promote the migration ability of photogenerated electrons. Our work provides new insights into approaches to enhance the photocatalytic CO_2 reduction activity of ZnO by adding carbon and loading with the transition metal cocatalyst Ni-NiS.

Conflicts of interest

The authors have no conflicts of interest to declare.

Acknowledgements

This work was supported by the National Key Research and Development Program of China (2018YFB1502001), the NSFC (51961135303, 51932007, 21871217, U1905215 and U1705251), the National Postdoctoral Program for Innovative Talents (BX20190259), the Innovative Research Funds of SKLWUT (2017-ZD-4), China Postdoctoral Science Foundation (2019M660189) and the Fundamental Research Funds for the Central Universities (WUT: 2019IVA111).

References

1 L. Buzzetti, G. E. M. Crisenza and P. Melchiorre, *Angew. Chem., Int. Ed.*, 2019, **58**, 3730–3747.
2 J. Low, B. Dai, T. Tong, C. Jiang and J. Yu, *Adv. Mater.*, 2019, **31**, 1802981.
3 C. Han, J. Li, Z. Ma, H. Xie, G. I. N. Waterhouse, L. Ye and T. Zhang, *Sci. China Mater.*, 2018, **61**, 1159–1166.
4 Q. Xu, B. Zhu, B. Cheng, J. Yu, M. Zhou and W. Ho, *Appl. Catal., B*, 2019, **255**, 117770.
5 A. Meng, B. Zhu, B. Zhong, L. Zhang and B. Cheng, *Appl. Surf. Sci.*, 2017, **422**, 518–527.
6 X. Meng, L. Liu, S. Ouyang, H. Xu, D. Wang, N. Zhao and J. Ye, *Adv. Mater.*, 2016, **28**, 6781–6803.
7 F. Xu, J. Zhang, B. Zhu, J. Yu and J. Xu, *Appl. Catal., B*, 2018, **230**, 194–202.
8 H. Wang, Y. Wang, L. Guo, X. Zhang, C. Ribeiro and T. He, *Chin. J. Catal.*, 2020, **41**, 131–139.
9 C. Bie, B. Zhu, F. Xu, L. Zhang and J. Yu, *Adv. Mater.*, 2019, **31**, 1902868.
10 S. Zhu and D. Wang, *Adv. Energy Mater.*, 2017, **7**, 1700841.
11 A. Meng, S. Wu, B. Cheng, J. Yu and J. Xu, *J. Mater. Chem. A*, 2018, **6**, 4729–4736.
12 J. Xiao, W. Yang, S. Gao, C. Sun and Q. Li, *J. Mater. Sci. Technol.*, 2018, **34**, 2331–2336.
13 T. Di, J. Zhang, B. Cheng, J. Yu and J. Xu, *Sci. China: Chem.*, 2018, **61**, 344–350.
14 H. Moussa, B. Chouchene, T. Gries, L. Balan, K. Mozet, G. Medjahdi and R. Schneider, *ChemCatChem*, 2018, **10**, 4973–4983.
15 J. Low, S. Qiu, D. Xu, C. Jiang and B. Cheng, *Appl. Surf. Sci.*, 2018, **434**, 423–432.
16 Q. Wang, W. Wang, L. Zhang, Y. Su, K. Wang and H. Wu, *J. Mater. Sci. Technol.*, 2018, **34**, 2337–2341.
17 G. T. S. T. da Silva, K. T. G. Carvalho, O. F. Lopes, E. S. Gomes, A. R. Malagutti, V. R. Mastelaro, C. Ribeiro and H. A. J. L. Mourão, *ChemCatChem*, 2017, **9**, 3795–3804.
18 S. Gao, W. Yang, J. Xiao, B. Li and Q. Li, *J. Mater. Sci. Technol.*, 2019, **35**, 610–614.
19 B. Zhu, Q. Zhang, X. Li and H. Lan, *Phys. Status Solidi A*, 2018, **215**, 1800359.
20 Y. Xu, C. Li, H. Huang, L. Huang, L. Peng and H. Pan, *Part. Part. Syst. Charact.*, 2019, **36**, 1800403.
21 F. Xu, B. Zhu, B. Cheng, J. Yu and J. Xu, *Adv. Opt. Mater.*, 2018, **6**, 1800911.
22 M. M. M. Melo, E. M. R. Rocha and E. L. Silva, *Environ. Qual. Manage.*, 2018, **28**, 65–71.
23 T. Xia, R. Long, C. Gao and Y. Xiong, *Nanoscale*, 2019, **11**, 11064–11070.
24 W. Yu, D. Xu and T. Peng, *J. Mater. Chem. A*, 2015, **3**, 19936–19947.
25 S. Wang, B. Zhu, M. Liu, L. Zhang, J. Yu and M. Zhou, *Appl. Catal., B*, 2019, **243**, 19–26.
26 Z. Guan, P. Wang, Q. Li, Y. Li, X. Fu and J. Yang, *Chem. Eng. J.*, 2017, **327**, 397–405.
27 M. Pirhashemi and A. Habibi-Yangjeh, *J. Mater. Sci. Technol.*, 2018, **34**, 1891–1901.
28 F. Xu, K. Meng, B. Zhu, H. Liu, J. Xu and J. Yu, *Adv. Funct. Mater.*, 2019, **29**, 1904256.

29 A. Meng, J. Zhang, D. Xu, B. Cheng and J. Yu, *Appl. Catal., B*, 2016, **198**, 286–294.
30 D. M. Fragua, R. Abargues, P. J. Rodriguez-Canto, J. F. Sanchez-Royo, S. Agouram and J. P. Martinez-Pastor, *Adv. Mater. Interfaces*, 2015, **2**, 1500156.
31 F. Xu, K. Meng, B. Cheng, J. Yu and W. Ho, *ChemCatChem*, 2019, **11**, 465–472.
32 D. Wu, K. Deng, B. Hu, Q. Lu, G. Liu and X. Hong, *ChemCatChem*, 2019, **11**, 1598–1601.
33 A. Meng, L. Zhang, B. Cheng and J. Yu, *Adv. Mater.*, 2019, **31**, 1807660.
34 H. Hao and X. Lang, *ChemCatChem*, 2019, **11**, 1378–1393.
35 T. Di, Q. Xu, W. Ho, H. Tang, Q. Xiang and J. Yu, *ChemCatChem*, 2019, **11**, 1394–1411.
36 Y. Yue, Y. Li, C. A. Bridges, G. Rother, J. Zhang, J. Chen, D. K. Hensley, M. K. Kidder, B. C. Richardson, M. Parans Paranthaman and S. Dai, *ChemNanoMat*, 2016, **2**, 1104–1110.
37 W. Tu, Y. Li, L. Kuai, Y. Zhou, Q. Xu, H. Li, X. Wang, M. Xiao and Z. Zou, *Nanoscale*, 2017, **9**, 9065–9070.
38 Y. Ren, D. Zeng and W.-J. Ong, *Chin. J. Catal.*, 2019, **40**, 289–319.
39 Z. Chen, S. Yang, Z. Tian and B. Zhu, *Appl. Surf. Sci.*, 2019, **469**, 657–665.
40 X. R. Zheng, X. P. Han, Y. Q. Zhang, J. H. Wang, C. Zhong, Y. D. Deng and W. B. Hu, *Nanoscale*, 2019, **11**, 5646–5654.
41 J. Wen, J. Xie, H. Zhang, A. Zhang, Y. Liu, X. Chen and X. Li, *ACS Appl. Mater. Interfaces*, 2017, **9**, 14031–14042.
42 D.-T. Nguyen, C.-C. Nguyen, M. St-Jean, S. Chabot, S. Kaliaguine and T.-O. Do, *ACS Appl. Nano Mater.*, 2018, **1**, 6864–6873.
43 Y. Zhong, J. Yuan, J. Wen, X. Li, Y. Xu, W. Liu, S. Zhang and Y. Fang, *Dalton Trans.*, 2015, **44**, 18260–18269.
44 J. Wen, X. Li, H. Li, S. Ma, K. He, Y. Xu, Y. Fang, W. Liu and Q. Gao, *Appl. Surf. Sci.*, 2015, **358**, 204–212.
45 C. Kong, S. Min and G. Lu, *ACS Catal.*, 2014, **4**, 2763–2769.
46 J. Wen, J. Xie, Z. Yang, R. Shen, H. Li, X. Luo, X. Chen and X. Li, *ACS Sustainable Chem. Eng.*, 2017, **5**, 2224–2236.
47 Q. Yu, R. Lin, L. Jiang, J. Wan and C. Chen, *Sci. China Mater.*, 2018, **61**, 1007–1011.
48 O. J. H. Chai, Z. Liu, T. Chen and J. Xie, *Nanoscale*, 2019, **11**, 20437–20448.
49 W.-N. Wang, F. Zhang, C.-L. Zhang, Y.-C. Guo, W. Dai and H.-S. Qian, *ChemCatChem*, 2017, **9**, 3611–3617.
50 Y. Sang, H. Liu and A. Umar, *ChemCatChem*, 2015, **7**, 559–573.
51 J. Low, L. Zhang, B. Zhu, Z. Liu and J. Yu, *ACS Sustainable Chem. Eng.*, 2018, **6**, 15653–15661.
52 W. Zhong, R. Sa, L. Li, Y. He, L. Li, J. Bi, Z. Zhuang, Y. Yu and Z. Zou, *J. Am. Chem. Soc.*, 2019, **141**, 7615–7621.
53 Z. Cheng, S. Zhao and L. Han, *Nanoscale*, 2018, **10**, 6892–6899.
54 S. Son, P.-H. Jung, J. Park, D. Chae, D. Huh, M. Byun, S. Ju and H. Lee, *Nanoscale*, 2018, **10**, 21696–21702.
55 H. Zhao, Y. Dong, P. Jiang, X. Wu, R. Wu and Y. Chen, *RSC Adv.*, 2015, **5**, 6494–6500.
56 Y. Sun, C. Liu, D. C. Grauer, J. Yano, J. R. Long, P. Yang and C. J. Chang, *J. Am. Chem. Soc.*, 2013, **135**, 17699–17702.
57 F. Xu, L. Zhang, B. Cheng and J. Yu, *ACS Sustainable Chem. Eng.*, 2018, **6**, 12291–12298.
58 Q. Xie, W. He, S. Liu, C. Li, J. Zhang and P. K. Wong, *Chin. J. Catal.*, 2020, **41**, 140–153.
59 N. Zhang, R. Long, C. Gao and Y. Xiong, *Sci. China Mater.*, 2018, **61**, 771–805.
60 Y. Tian, L. Zhou, Q. Zhu, J. Lei, L. Wang, J. Zhang and Y. Liu, *Nanoscale*, 2019, **11**, 20638–20647.
61 R. Amiruddin and M. C. S. Kumar, *J. Lumin.*, 2014, **155**, 149–155.
62 Z.-q. Zhu and J. Zhou, *Int. J. Miner., Metall. Mater.*, 2010, **17**, 80–85.